Journal of Solid State Chemistry 181 (2008) 2424–2432

Contents lists available at ScienceDirect

Journal of Solid State Chemistry

journal homepage: www.elsevier.com/locate/jssc

Preparation and characterization of (SBA-15)–La_2O_3 host–guest composite materials

Hui Yu, Qing-Zhou Zhai *

Research Center for Nanotechnology, Changchun University of Science and Technology, Changchun 130022, Jilin Province, PR China

ARTICLE INFO

Article history:
Received 28 February 2008
Received in revised form
15 May 2008
Accepted 1 June 2008
Available online 5 June 2008

Keywords:
Mesoporous SBA-15 molecular sieve host
Lanthanum oxide guest
Host–guest composite material
Liquid-phase grafting
Thermal diffusion
Microwave-assisted synthesis
Characterization
Optical property

ABSTRACT

Lanthanum oxide was successfully incorporated into an SBA-15 mesoporous molecular sieve via the microwave-assisted synthesis method (MASM) for the first time, and was compared with liquid-phase grafting and thermal diffusion methods. A series of characterizations were used to characterize the prepared materials. The results showed that the preparation of (SBA-15)–La_2O_3 host–guest composite materials by MASM has the advantages of simpler operation, higher efficiency and more plentiful lanthanum oxide could be incorporated into SBA-15 compared with other methods. In the prepared host–guest (SBA-15)-La_2O_3 materials, the frameworks of the host molecular sieve were kept intact, their structures were still kept high ordered and the guest lanthanum oxide locates inside the pores of the SBA-15. The sizes of the prepared (SBA-15)–La_2O_3 samples were 340–357 nm. The prepared host–guest composite materials show the properties of luminescence, and the luminescent intensities are about 2 times of bulk La_2O_3.

1. Introduction

In 1992, researchers of Mobil published a breakthrough report on the synthesis of ordered mesoporous silica materials [1]. The publications of these results have stimulated a large and world-wide effort to synthesize new types of ordered mesoporous materials. Due to their controlled pore size and a very narrow pore size distribution, the ordered mesoporous materials have a large potential as catalytic supports in the chemical industry [2], pharmaceutical production [3] and the production of special polymer materials [4]. Unfortunately, the actual use of the molecular sieve has been severely hampered by their poor stability. SBA-15 is a material that has a 2D hexagonal arrangement of pores. It has the benefits of a combined microporosity and mesoporosity and relatively thick walls [5]. The enhanced chemical and thermal stability of the material, compared with MCM-41, can be ascribed to the thicker pore walls of the SBA-15 materials and attracts much interest [6]. Silica-based mesoporous materials with high surface area are of great interest as host materials for growing the nanoscale guest materials confined inside the nanopores of the hosts. These guest materials deal with polymers, metals and semiconductors that have potential ability in catalytic, environmental, photoelectrical materials and other applications [7]. Specially, an SBA-15 molecular sieve with a bigger pore size adapts to be used as a template for producing nanoscale materials. A number of inclusion techniques have been developed in the past, such as wet impregnation [8], solid-state diffusion [9], covalent grafting [10] and co-condensation [11]. The impregnation method has been used to prepare Fe_2O_3, Ga_2O_3, In_2O_3, Cu_2O and $CsLaO_2$ nanoparticles inside the channels of MCM-41 [12,13], and Ag, Au, Pt, Pd, Rh, Si nanowires inside the channels of SBA-15 [14], HMM [15] or MCM-41 [16]. The liquid-phase grafting method is based on the weak interaction between basic organic metal precursors and acidic silanol groups on the internal surface of mesoporous materials, which has been used to synthesize titania in MCM-41 [17] and zirconia in MCM-48 [18]. One-dimensional V_2O_5 nanowires have been synthesized inside the channels of mesoporous SBA-15 through the chemical approach, which involves aminosilylation of silanol groups on the silica surface, anchoring of isopoly acid, $H_6V_{10}O_{28}$, by neutralization of basic amine groups, and thermal decomposition [19]. The microwave-assisted synthesis of molecular sieves is a relatively new area of research [20]. This method has been successfully applied to the synthesis of several types of zeolites, such as Co-CHA, Co-AFI [21], $AlPO_4$-5 [22], Beta [23], Y, ZSM-5 [24], MCM-41 [25] and $AlPO_4$, Cloverite [26]. Microwave-assisted synthesis of molecular sieves offers many distinct advantages over conventional synthesis. These advantages include (1) heat to crystallization temperature rapidly, (2) volumetric heating results

* Corresponding author. Fax: +86 431 85383815.
E-mail addresses: zhaiqingzhou@163.com, zhaiqingzhou@hotmail.com (Q.-Z. Zhai).

0022-4596/$ - see front matter © 2008 Elsevier Inc. All rights reserved.
doi:10.1016/j.jssc.2008.06.001

in homogeneous nucleation, (3) fast supersaturate by the rapid dissolution of precipitated gels, and (4) a shorter crystallization time compared with conventional autoclave heating. Furthermore, it is energy efficient and economical [27]. As Bharat and coworkers reported, titanium-substituted mesoporous SBA-15 molecular sieve has been successfully prepared at 373 K by direct synthesis under microwave-hydrothermal conditions within about 2 h [28].

This paper presents a study that an SBA-15 molecular sieve was doped with La_2O_3 via three pathways including the thermal diffusion method, the liquid-phase grafting method and the microwave-assisted synthesis method (MASM). Powder X-ray diffraction, chemical analysis, nitrogen adsorption–desorption technique, infrared spectroscopy, solid-state diffuse reflection absorption spectra and luminescence spectra studies were used to evaluate the samples. These characterizations showed that La_2O_3 has been successfully incorporated inside the channels of the SBA-15 molecular sieve.

2. Experimental

2.1. Chemicals

Tetraethyl orthosilicate (TEOS, 98%, Fluka), poly(ethylene glycol)-block-poly(propylglycol)-block-poly(ethylene glycol) ($EG_{20}PG_{40}EG_{20}$, Aldrich), lanthanum oxide (A.R., Beijing Research Institute of Rare Earths, China) and lanthanum nitrate (A.R., Shanghai Chemical Reagent Corporation of Chinese Medicine Group). A 2 mol/L hydrochloric acid solution was prepared from concentrated hydrochloric acid (A.R.) by suitable dilution. The water used in experiments was deionized water

2.2. Preparation of SBA-15 molecular sieve

Mesoporous SBA-15 molecular sieve was prepared according to the procedure of Ref. [5]. In the acidic condition, the triblock copolymer, $EG_{20}PG_{40}EG_{20}$, was used as a template and TEOS was used as the silicon source. In a typical synthesis, 2.0 g of the template was dissolved in 60 g of 2 mol/L hydrochloric acid and 15.0 g of deionized water, then 4.25 g of TEOS was added, stirred for 24 h at 40 °C. The mixture was aged in a Teflon-liner autoclave treated at 100 °C for 48 h. The product was filtered and washed with deionized water and dried at room temperature. The obtained material was calcined at 550 °C for 24 h to completely eliminate the template. The sample was designed as S.

2.3. Loading of La_2O_3

The loading of La_2O_3 was achieved by three pathways: (a) 0.5 g of the mesoporous SBA-15 molecular sieve was immersed in 30 mL of 0.1 mol/L lanthanum nitrate aqueous solution and stirred for 24 h at temperature 60 °C. The solid product was filtered off, washed with deionized water and dried at room temperature. The sample was calcined at 800 °C for 6 h. Then the sample was cooled down to room temperature in oven. The sample was designed as LS (liquid-phase grafting method loaded La_2O_3 into SBA-15). (b) 0.5 g of the SBA-15 was mixed with 0.0556 g lanthana to make the mixture homogeneous. The mixture was calcined at 500 °C for 48 h. Then, the sample was cooled down to room temperature in an oven. The sample was designed as SS (solid-phase thermal diffusion method loaded La_2O_3 into SBA-15). (c) MASM: (i) 0.5 g of the SBA-15 was mixed with 0.0556 g lanthana to make the mixture homogeneous. The mixture was irradiated by microwave for 30 min at 750 W in a microwave oven. Then, the sample was cooled down to room temperature in the oven. The sample was designed as MWSS (MASM loaded La_2O_3 into SBA-15 from **s**olid La_2O_3). (ii) 0.5 g of the SBA-15 was mixed with 0.1109 g lanthanum nitrate to make the mixture homogeneous. The mixture was irradiated by microwave for 30 min at 750 W. Then, the sample was cooled down to room temperature in the oven. The sample was washed with deionized water, filtered and dried at room temperature. Finally, the sample was calcined at 800 °C for 6 h and cooled down to room temperature in an oven. The sample was designed as MWNS (MASM loaded La_2O_3 into SBA-15 from lanthanum nitrate).

2.4. Characterization

X-ray powder diffraction (XRD) patterns were collected on a Siemens D5005 diffractometer using Cu-$K\alpha$ radiation ($\lambda = 1.5418$ Å and operating at 30 kV and 20 mA). Fourier transform infrared (FT-IR) spectra were obtained using a Bruker Vertex 70 FT-IR spectrometer. Powder samples (1 wt%) were dispersed in KBr (99 wt%) pellets for IR analysis. Adsorption–desorption study of nitrogen was performed on a Micromeritics ASAP2010 M volumetric adsorption analyzer at 77 K. A sample was degassed in vacuum at 573 K for 12 h before measurement. The surface area was calculated based on the BET (Brunner–Emmett–Teller) method [29], while pore size distribution was computed using the BJH (Barrett–Joyner–Halenda) method [30]. Transmission electron microscopy (TEM) images were taken on a JEOL 2010 TEM instrument. Scanning electron microscopy (SEM) images were recorded on a JEOL JSM-5600L SEM instrument. Determination of lanthanum content was carried out with *p*-acetylarsenazo by spectrophotometry [31]. Determination of silicon in molecular sieves was made by molybdosilicate blue photometry [32]. Spectrophotometric determinations of silicon and lanthanum were carried out on a 722 spectrophotometer. UV–vis diffuse reflectance spectra were measured on a UV-4100 spectrophotometer (Hitachi) converted by the online instrument system for data acquisition and analysis using PC. Luminescence spectra were collected on an SPEX-FL-2T2 luminescence spectrometer at room temperature.

3. Results and discussion

3.1. Chemical analysis

The contents of Si and La were obtained by spectrophotometry. The oxygen content was obtained by the difference subtraction method (Table 1). The results showed that the molecular formula of samples SS was $La_2Si_{64}O_{131}$, of MWSS was $La_2Si_{51}O_{105}$, of MWNS was $La_2Si_{99}O_{201}$ and of LS was $La_2Si_{83}O_{169}$, respectively. It can be seen that La_2O_3 has been incorporated into the SBA-15 molecular sieve.

3.2. Powder X-ray diffraction (XRD)

Fig. 1A shows the small-angle XRD patterns of the prepared samples. The sample S possesses four reflection peaks denoted as

Table 1
Content of elements and Si /La in samples

Samples	La (wt%)	Si (wt%)	O(wt%)	Si/La (in molar ratio)
SS	6.7	43.0	50.3	32
MWSS	8.3	42.1	49.6	25
MWNS	4.4	44.3	51.3	49
LS	5.2	43.8	51.0	41

(100), (110), (200) and (210), respectively, and these peaks belong to those of the SBA-15 molecular sieve [5]. The samples SS, MWNS, MWSS and LS exhibit three characteristic peaks of the SBA-15 molecular sieve, indicating that the hexagonal pore structure of the SBA-15 molecular sieve structure is conserved after the inclusion of La_2O_3. The structures of the SBA-15 in the host–guest (SBA-15)–La_2O_3 materials keep a much higher order state for the samples of SS and MWSS than those of samples LS and MWNS. It shows that its breakage to the SBA-15 molecular sieve by thermal diffusion and MASM are smaller than that by the liquid-phase grafting method after the inclusion of La_2O_3. The peaks of (100), (110) and (200) reflections of SS, MWNS, MWSS and LS slightly shift to higher angles in comparison with those of the sample S (Fig. 1A), which accounts for the contraction of the host framework during incorporation of lanthanum oxide.

Fig. 1B illustrates the wide-angle XRD patterns of samples SS, MWNS, MWSS, LS, bulk La_2O_3 and a mechanical mixture of SBA-15 and La_2O_3 (5 wt%). All reflections of La_2O_3 are seen for the mechanical mixture of SBA-15 and La_2O_3. No reflections of La_2O_3 are seen for samples MWNS and LS. It indicates that La_2O_3 exists in the pores with monolayer molecules, but not on the external surface of the SBA-15 molecular sieve. The partial weak reflections of La_2O_3 are seen for samples SS and MWSS. It can be explained that when a loading amount becomes higher, a small quantity of La_2O_3 exists with crystal.

3.3. Fourier transform infrared spectra

Infrared spectroscopy can reflect the change of configuration of the frameworks of molecular sieve host after the incorporation of the guests into the molecular sieve. Fig. 2 shows the FT-IR spectra of each sample. From the FT-IR analysis, it is found that no structural collapse of pore structures occurred by the incorporation of lanthanum oxide or its precursors for Si–O bonds.

In the IR pattern (Fig. 2), each sample has three peaks for (SBA-15)–La_2O_3 samples and the SBA-15 molecular sieve. The bands that locate at 466, 468, 467, 468 and 466 cm^{-1} correspond to T–O bending. The bands that locate at 804, 804, 810, 806 and 802 cm^{-1} correspond to symmetric stretching. The bands that locate at 1092, 1091, 1090, 1097 and 1090 cm^{-1} correspond to asymmetric stretching [33]. The addition of La_2O_3 guest component weakens the peak intensities of 1090 cm^{-1} of the SBA-15 molecular sieve. However, the change in intensity of the peak is different according to the La_2O_3 incorporated amount. In the (SBA-15)–La_2O_3 samples, the La_2O_3 components incorporated excessively into SBA-15 attack the Si–O bonding in the mesoporous framework. In addition, the peaks for SS, MWSS, MWNS and LS samples shift to higher wavenumbers in comparison with those of the SBA-15 molecular sieve. A similar shift has been observed for Eu-doped MCM-41 [11].

In the IR pattern (Fig. 2), bulk La_2O_3 sample has only one peak that is located at 640 cm^{-1}. The mechanical mixture of SBA-15 and

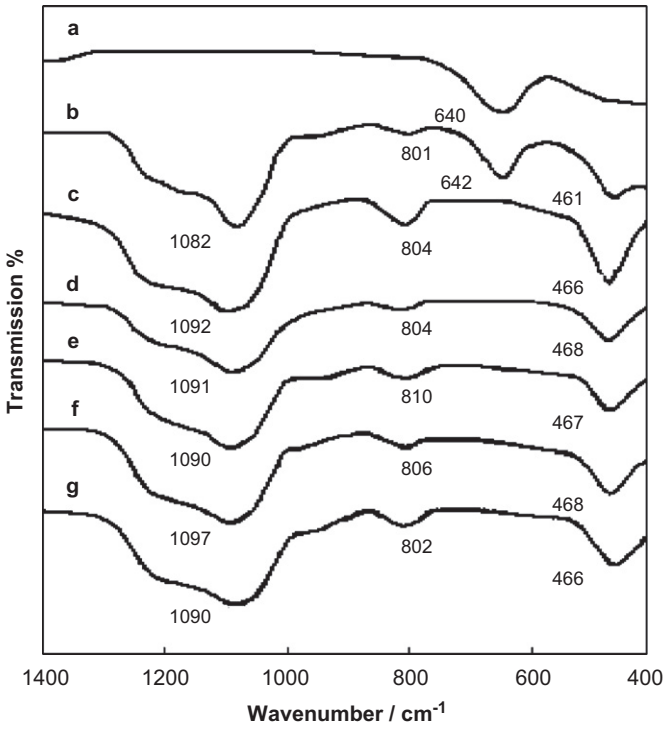

Fig. 2. Infrared spectra of each sample (a) La_2O_3, (b) mechanical mixture of SBA-15 and La_2O_3 (5 wt%), (c) SS (thermal diffusion), (d) MWSS (microwave La_2O_3 diffusion), (e) MWNS (microwave $La(NO_3)_3$ diffusion), (f) LS (liquid phase grafting), (g) SBA-15.

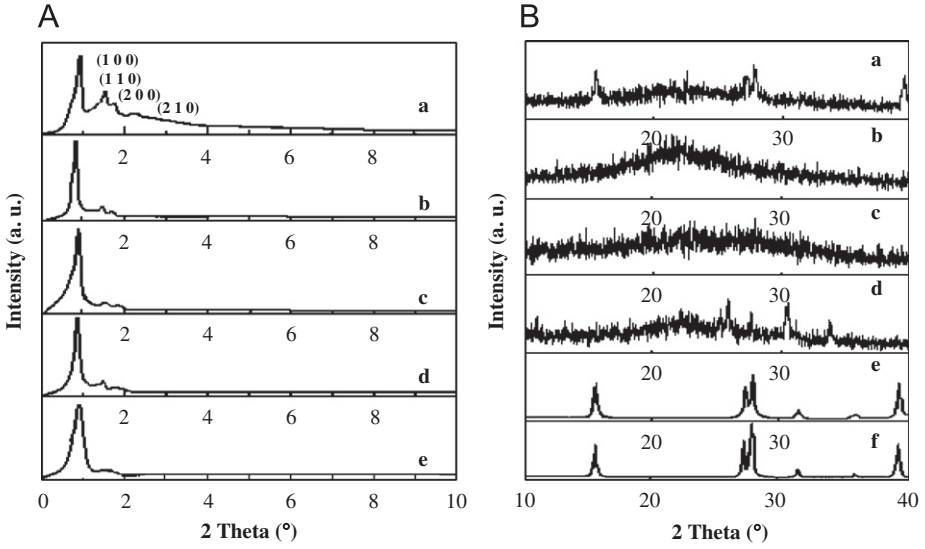

Fig. 1. (A) Small-angle XRD patterns of: (a) SBA-15, (b) SS (thermal diffusion), (c) MWNS (microwave $La(NO_3)_3$ diffusion), (d) MWSS (microwave La_2O_3 diffusion), (e) LS (liquid phase grafting); (B) wide-angle XRD patterns of: (a) heat diffusion—SBA-15–La_2O_3 (SS), (b) microwave $La(NO_3)_3$ diffusion—SBA-15–La_2O_3 (MWNS), (c) microwave La_2O_3 diffusion—SBA-15–La_2O_3(LS), (d) liquid-phase—SBA-15–La_2O_3 (MWSS), (e) La_2O_3, (f) mechanical mixture of SBA-15 and La_2O_3 (5 wt%).

La_2O_3 (5 wt%) has four peaks that locate at 1082, 801, 642 and 461 cm^{-1}, respectively. For the mechanical mixture of SBA-15 and La_2O_3 (5 wt%), the bands that locate at 1082, 801 and 461 cm^{-1} correspond to SBA-15 characteristic peaks and that locate at 642 cm^{-1} corresponds to the characteristic peak of the La_2O_3 guest. IR patterns of (SBA-15)–La_2O_3 samples are similar to those of the SBA-15, characteristic IR peaks of La_2O_3 do not appear. It might be interpreted that the La_2O_3 components doped in the pores, or equably dispersed on the surface of SBA-15.

3.4. Low-temperature nitrogen adsorption– desorption isotherms

Low-temperature nitrogen adsorption–desorption isotherms are commonly used to evaluate the pore structure parameters of mesoporous materials. Fig. 3A shows the low-temperature N_2 adsorption–desorption isotherms of the samples. The isotherms of all samples show typical irreversible type IV adsorption isotherms with a H1 hysteresis loop, which are characteristic of mesoporous materials with 1-D cylindrical channels as defined by IUPAC [34]. The isotherms of the samples featured hysteresis loops with sharp adsorption and desorption branches. The sharpness of the adsorption branches is indicative of a narrow mesopore size distribution as Fig. 3B. At low partial pressures (P/P_0), the adsorption is mainly monolayer adsorption. There are no pore-blocking effects from narrow pores during desorption, and the capillary condensation cannot occur at relative lower pressures. Therefore the hysteresis feature does not appear. The adsorption is multilayer adsorption as relative pressure increases and adsorptive quantity increases. However, the volumes adsorbed inflected sharply at relative pressure (p/p_0) 0.73 for SBA-15, 0.65 for MWSS and SS, 0.6 for MWNS, 0.58 for LS. It can be explained that the relative pressure increases to the degree that capillary condensation occurred. The difference between adsorption and desorption process can conclude that adsorption and desorption are irreversible, desorption lag to adsorption process. The most possible reason is due to the effect of constrictions in the cylindrical mesopores, which would cause the delayed capillary evaporation [35,36]. So the adsorption and desorption processes may progress under different relative pressures [37]. In the case of mesopores, the capillary condensation pressure is an increasing function of the pore diameter. The amount of adsorbed nitrogen decreases and the onset of the capillary condensation step shifts to relative lower pressures. The decrease in the amount of adsorbed N_2 can be attributed to the reduced pore volume and the condensation in the adsorption branch starting at lower p/p_0 is caused by the smaller pore size. Nevertheless, it should be noted that the hysteresis in the high-pressure range corresponds to the mesoporosity character of SBA-15, confirming that La_2O_3 nanowires are located inside the channels and the mesoporous channels still remain. When the relative pressure is higher than 0.85 for SBA-15, 0.9 for MWSS and SS, 0.85 for MWNS and 0.8 for LS, the hysteresis does not appear. It is because the adsorption and desorption processes mainly carry out on the outer surface, and the processes are reversible.

The calculated surface areas and the mesopore parameters based on the Barrett, Joyner and Halenda (BJH) [29,30] analysis are calculated from the adsorption branch of nitrogen adsorption–desorption isotherms. The surface areas, average pore diameter and mesopore volume decreased with the incorporation

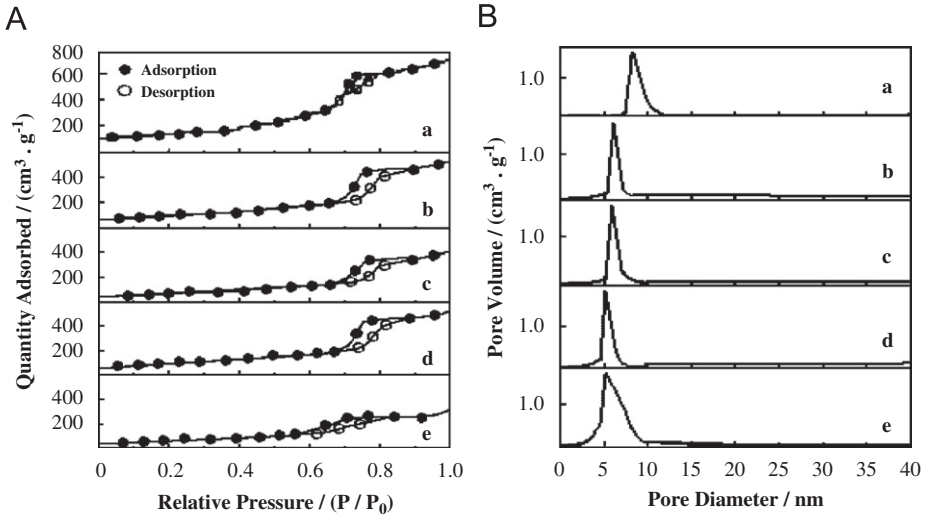

Fig. 3. (A) Low-temperature nitrogen adsorption–desorption isotherms (●, adsorption; ○, desorption). (B) Pore size distribution patterns of samples: (a) SBA-15, (b) MWSS (microwave La_2O_3 diffusion), (c) SS (thermal diffusion), (d) MWNS (microwave $La(NO_3)_3$ diffusion), (e) LS (liquid phase grafting).

Table 2
Pore structure parameters of samples

Sample	d_{100}/nm	a_0[a]/nm	Surface (area/$m^2\,g^{-1}$)	Pore (volume[b]/$cm^3\,g^{-1}$)	Pore (size[c]/nm)	NSA
S	9.56	11.04	594.7	1.059	8.14	–
MWSS	10.01	11.56	537.3	0.832	7.29	1.01
SS	10.51	12.13	425.7	0.894	7.07	0.78
MWNS	9.81	11.07	433.1	0.848	6.07	0.77
LS	9.59	11.32	366.8	0.883	6.01	0.66

[a] $a_0 = (2/\sqrt{3})d_{100}$.
[b] BJH adsorption cumulative volume of pores.
[c] Pore size calculated from the adsorption branch.

of the La_2O_3 component. As is shown in Table 2, for MWSS, SS, MWNS and LS, the average pore diameters decreased from 8.14 to 7.29, 7.07, 6.07 and 6.01 nm, the surface area decreased from 594.7 to 537.3, 425.7, 433.1 and 366.8 m^2/g, the pore volume decreased from 1.059 to 0.832, 0.636, 0.569 and 0.484 cm^3/g, respectively. Accordingly, the filling of the channels after addition of the La_2O_3 component decreased the pore volume, pore size and surface area.

In order to quantify the possible SBA-15 pore blocking by the La_2O_3 , the normalized surface area (NSA) is defined as [38]

$$\mathrm{NSA} = \frac{\mathrm{SA}_1}{1-y}\frac{1}{\mathrm{SA}_2} \quad (1)$$

where SA_1 and SA_2 are surface areas of the parent SBA-15 and (SBA-15)–La_2O_3 composite, y is weight fraction of the La_2O_3 in the sample.

In the present study, the NSA values are 1.01, 0.78, 0.77 and 0.66 for MWSS, SS, MWNS and LS samples, respectively. MWSS has an NSA$\sim$1, so it is in the form of an amorphous layer that covers the SBA-15 pore surface. For SS, MWNS and LS samples, they have an NSA$\ll$1, so guest phases in form of large particles at least partially located inside the SBA-15 pores while blocking them significantly. This brings on descending surface area, pore volume and pore size. The guest phase forms a new surface but shields the surface of the parent SBA-15, so that the NSA is close to

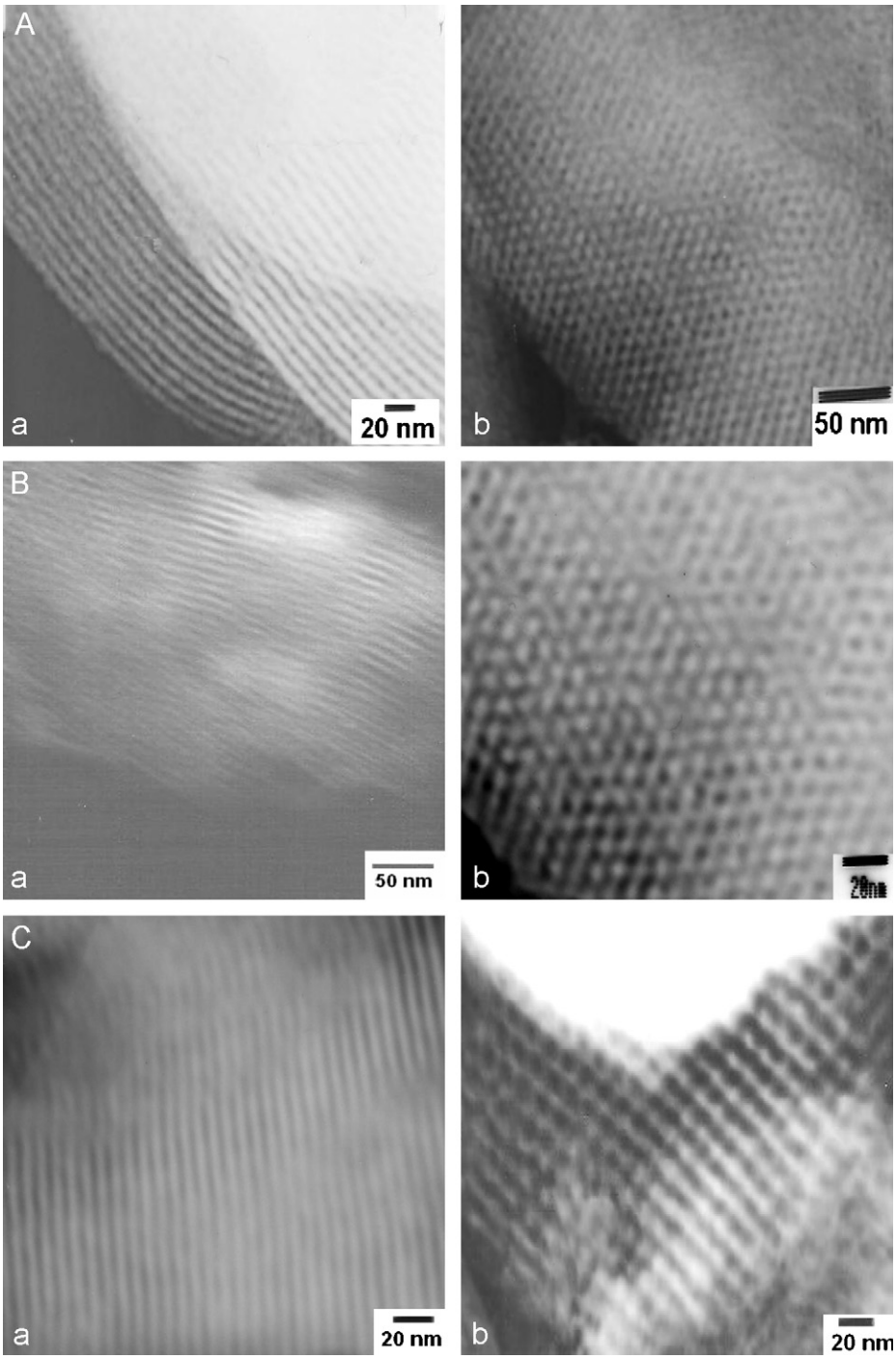

Fig. 4. TEM image of (A) SBA-15, (B) MWSS (microwave La_2O_3 diffusion), (C) SS (thermal diffusion), (D) MWNS (microwave $La(NO_3)_3$ diffusion), (E) LS (liquid phase grafting) (a) taken with the beam direction parallel to the pores and, (b) taken with the beam direction perpendicular to the pores.

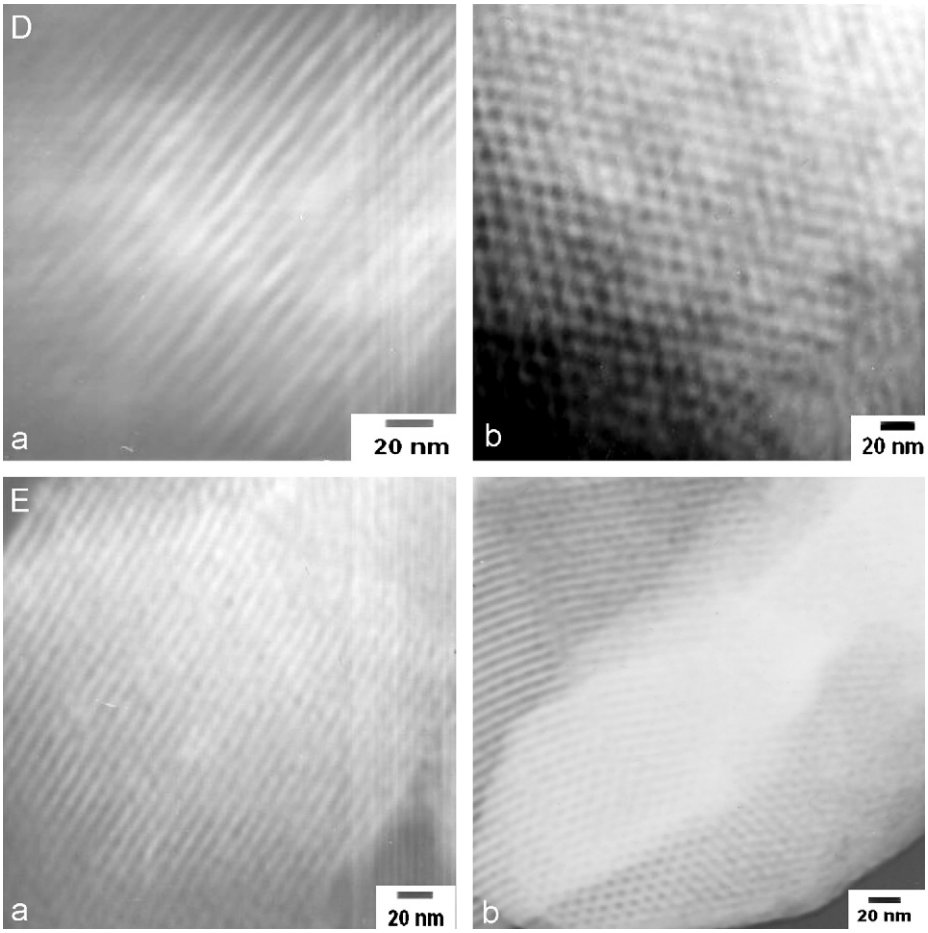

Fig. 4. (*Continued*)

unity [38]. These results are coincident with those of nitrogen adsorption–desorption isotherms.

Microwave-assisted synthesis offers many distinct advantages: (i) Heat to crystallization temperature rapidly; (ii) volumetric heating results in homogeneous nucleation; (iii) fast supersaturate by the rapid dissolution of precipitated gels; and (iv) a shorter crystallization time compared with conventional autoclave heating. These advantages make the MWSS sample have guest phases in the form of smaller particles, and cover the SBA-15 pore surface homogeneously.

3.5. Transmission electron microscopy

All TEM micrographs are recorded with the electron beam direction parallel to and perpendicular to the channel direction. The results (Fig. 4) show the well-ordered hexagonal arrays of mesopores and straight lattice fringes from the images viewed along and perpendicular to the pore axis, confirming the existence of a 2-D hexagonal structure of a *p*6*mm* symmetry. TEM images show that the highly ordered mesoporous structures of the SBA-15 remain after the formation of La_2O_3 inside the SBA-15 channels. Moreover, small clusters encapsulated inside the mesoporous channels can also be discerned and no large particles located outside the mesopores are observed.

3.6. Scanning electron microscopy

SEM analyses of the samples (Fig. 5) show the primary particles of the samples present a fibriform form. SBA-15 particle diameter is 333 nm, (SBA-15)–La_2O_3 sample diameters are 357 nm for MWSS, 345 nm for SS, 345 nm for MWNS and 340 nm for LS, respectively. SBA-15 particles have a smaller particle size than the (SBA-15)–La_2O_3 samples. The fibriform particles of the prepared samples still remain.

3.7. Optical properties

3.7.1. UV–vis solid diffusion reflectance spectra

The UV–vis solid diffuse reflectance spectra of the La_2O_3, mechanical mixture of the SBA-15 and La_2O_3 (5 wt%), SBA-15 and (SBA-15)–La_2O_3 are shown in Fig. 6. There is no absorption over the wavelength range of 200–800 nm for the molecular sieve SBA-15. A main absorption band shows at 268 nm for guest La_2O_3, which is assigned to low-energy oxygen-to-metal charge transfer band. A much weak absorption band shows at 270 nm for the mechanical mixture of SBA-15 and La_2O_3 (5 wt%), which corresponds to the absorption of guest La_2O_3. For the samples of SS, MVSS, MVNS and LS, one main absorption peak showed, respectively, which corresponds to the absorption of nanometer guest La_2O_3 located in the pore channels of the SBA-15. Therefore, the absorption of the (SBA-15)–La_2O_3 is not affected by the host molecular sieve. However, the absorption bands shift to 232, 257, 256 and 251 nm. The onset of absorption for the (SBA-15)–La_2O_3 material is obviously blue-shifted 36, 11, 12 and 18 nm relative to that of the bulk La_2O_3, respectively. The absorptions are caused by the nanosized La_2O_3, which are confined by the channels of the SBA-15. The blue-shift phenomenon can be ascribed to the stereoconfinement of the

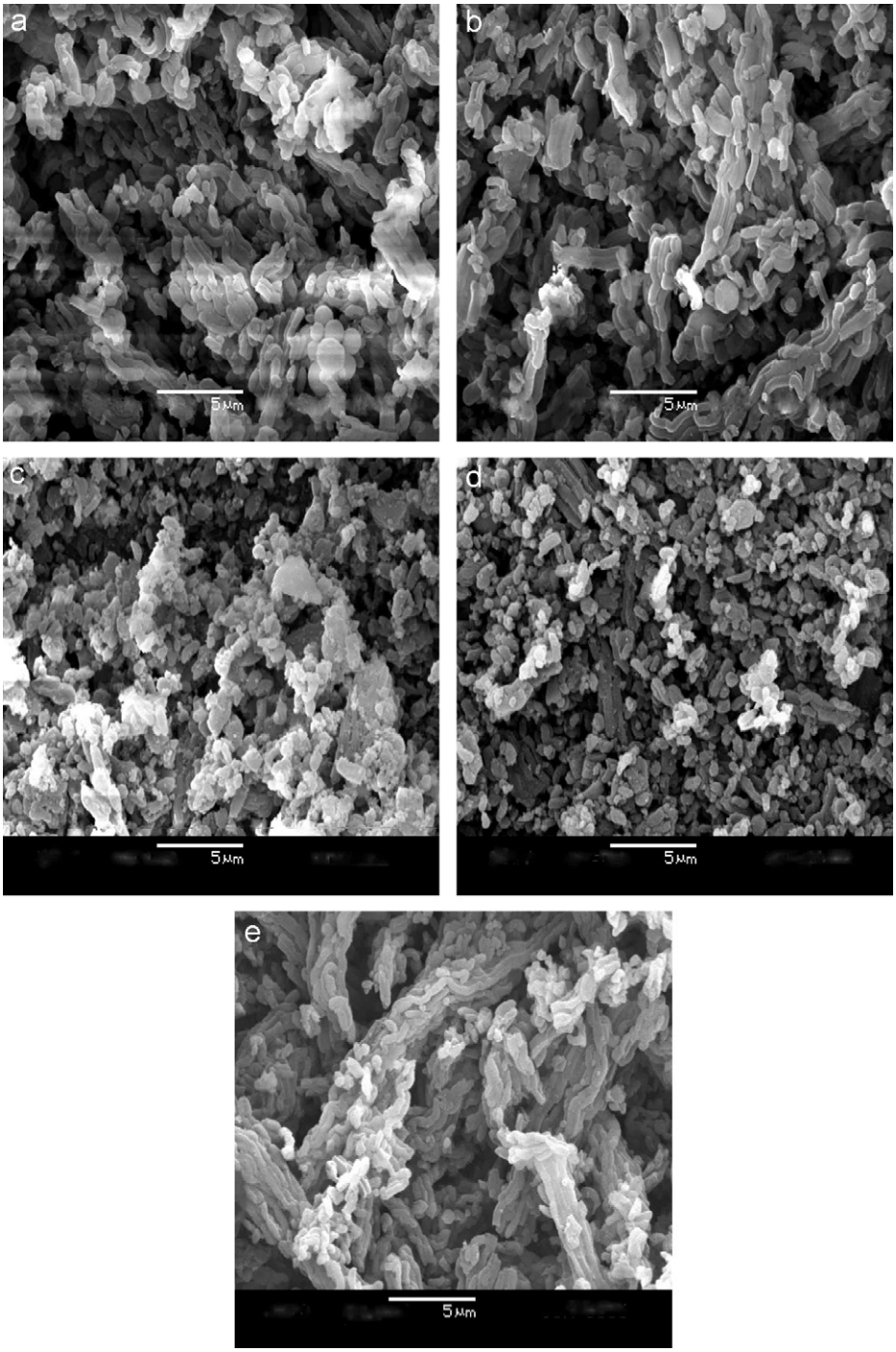

Fig. 5. SEM image of (a) SBA-15, (b) MWSS (microwave La_2O_3 diffusion), (c) SS (thermal diffusion), (d) MWNS (microwave $La(NO_3)_3$ diffusion), (e) LS (liquid phase grafting).

pores of the SBA-15 and quantum size effect is clearly associated with the nanosize of La_2O_3. The absorption of (SBA-15)–La_2O_3 shows that the energy of the forbidden bands of lanthanum oxide are increased. From the theory of quantum mechanics, if the particle size is smaller, the change in energy of the forbidden band is more. The particle size of La_2O_3 is smaller, the energy of the exciting electron and hole of La_2O_3 are higher. Thus, this phenomenon is caused in the solid-state diffuse reflectance absorption spectra of samples. The solid-state diffuse reflectance absorption spectra prove that La_2O_3 had been successfully trapped in the channels of the SBA-15 molecular sieve.

3.7.2. Luminescence

The excitation and emission spectra can provide information on energy bands, surface states, defects, etc. The luminescence spectra of the samples are shown in Fig. 7. The reported spectra are corrected automatically for the photomultiplier response and all the measurements were carried out at room temperatures and under the same conditions. There are no phenomena of luminescence of the host SBA-15 molecular sieve. However, for the prepared (SBA-15)–La_2O_3 composite materials, the phenomena of luminescence appeared. The excitation peaks of the bulk La_2O_3, SS, MWSS, MWNS and LS are at 210, 223, 219, 216 and 228 nm, respectively. The corresponding emission peaks are at 349, 397,

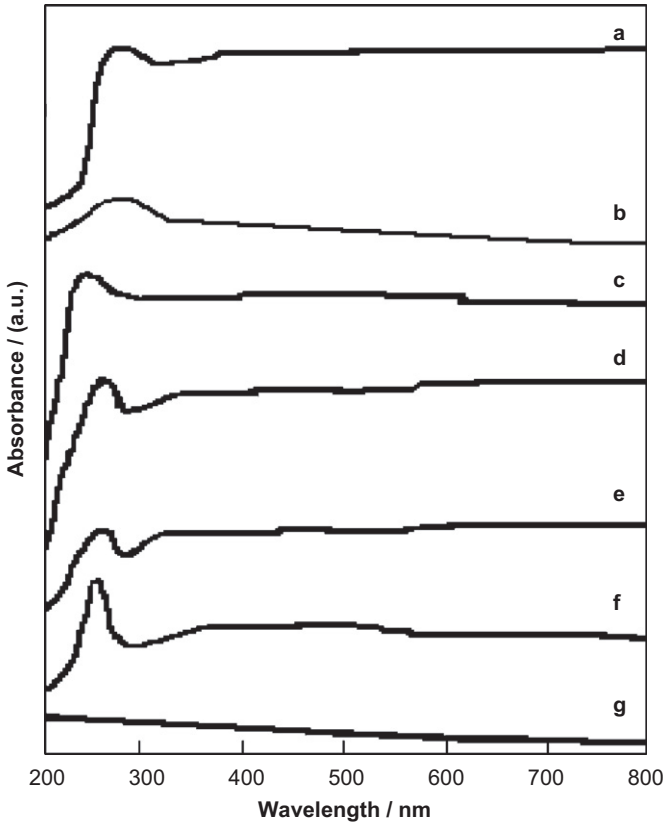

Fig. 6. UV–vis diffuse reflectance spectra of: (a) La_2O_3, (b) mechanical mixture of SBA-15 and La_2O_3 (5 wt%), (c) SS (thermal diffusion), (d) MWSS (microwave La_2O_3 diffusion), (e) MWNS (microwave $La(NO_3)_3$ diffusion), (f) LS (liquid phase), (g) SBA-15.

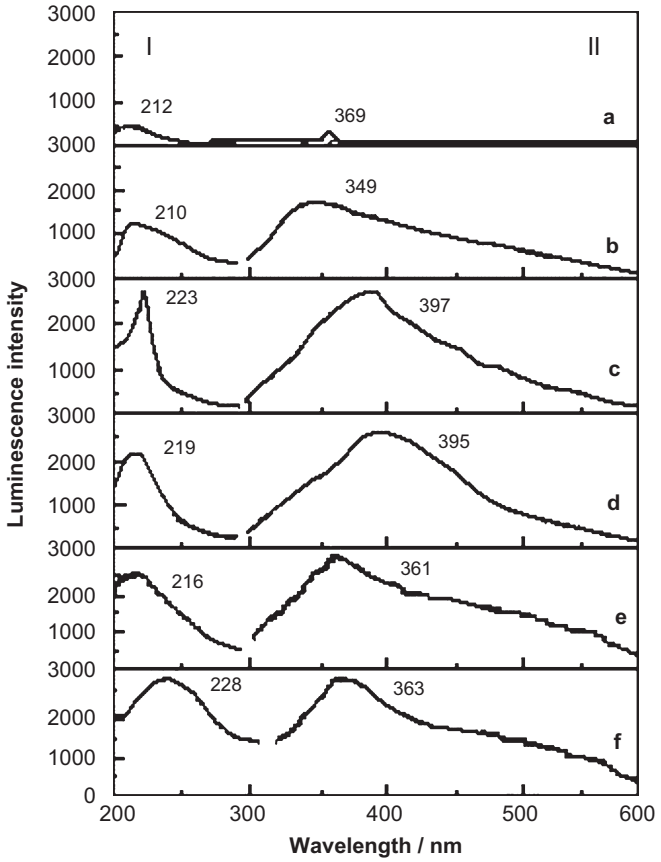

Fig. 7. The luminescence spectra of (a) mechanical mixture of SBA-15 and La_2O_3 (5 wt%), (b) La_2O_3, (c) heat diffusion—SBA-15–La_2O_3(SS), (d) microwave La_2O_3 diffusion—SBA-15–La_2O_3(MWSS), (e) microwave $La(NO_3)_3$ diffusion—SBA-15–La_2O_3 (MWNS), (f) liquid-phase—SBA-15–La_2O_3 (LS). (I) Excitation spectrum (II) emission spectrum.

395, 361 and 363 nm, respectively. The excitation and emission peaks of the mechanical mixture of SBA-15 and La_2O_3 (5 wt%) are at 212 and 369 nm, respectively. It is well known that there are no 4f electrons ($4f^0$) for La^{3+}, $f \rightarrow f$ transition cannot appear. Thus, La^{3+} belongs to an inert optical element, and it shows a weak luminescence spectrum in the ultraviolet region. The luminescence spectrum is zonary, which is brought by $L^* \rightarrow L$ [39]. The luminescent intensities of the samples are weak, which shows that the non-radiative process is very strong. And the population inversion is very easily established. The strong interaction of electron–photon in the samples induces the Stokes displacement and broadens the spectra bands. The luminescent intensities of the SS, MWSS, MWNS and LS samples are about 2 times of bulk La_2O_3 and 6 times of the mechanical mixture of SBA-15 and La_2O_3. It can be explained that oxygen-vacant sites in the (SBA-15)–La_2O_3 composite materials promote the formation of a more active chemisorbed species that contributes to the enhancement of reaction rate as compared to pure lanthana [40]. The excitation spectra of the samples are related to the La_2O_3 excitation, for which electronic transitions from the O ($2p$) valence band to the La ($5d6s$) conduction band (La_2O_3 lattice absorption). In addition, the energy difference changes, which can cause the difference of the surface defects at the surface of the materials. These defects may increase the degree of disorder and local symmetry of La_2O_3 located in the pores of the SBA-15 [41–43]. La_2O_3 is incorporated into the nanopores of the SBA-15 mesoporous molecular sieve that made molecules of La_2O_3 arrange tidily and kinetic energy decrease. The decreasing kinetic energy increases the luminescent intensities of the composite materials, and peaks of the excitation and emission spectra remove to bigger wavelength.

4. Conclusions

The combination of a series of characterization techniques has demonstrated that La_2O_3 can be doped inside the pores of the mesoporous SBA-15 molecular sieve. The results showed that the frameworks of the prepared (SBA-15)–La_2O_3 composite materials were intact, the mesoscopic ordering degrees were still very high and were kept high ordered. The preparation of the (SBA-15)–La_2O_3 host–guest composite materials by MASM has the advantages of simpler operation, higher efficiency and more plentiful lanthanum oxide can be incorporated into the SBA-15 compared with other methods. The MASM can also be used to incorporate other materials into the channel of mesoporous silica for specific applications. The solid-state diffuse reflectance absorption spectra of the prepared host–guest nanocomposite materials show blue shift relative to that of the bulk La_2O_3, suggesting that La_2O_3 was trapped in the channels of the molecular sieve. The channels of the molecular sieves in the composite materials have an obvious stereoscopic confinement effect on the La_2O_3. The prepared host–guest composite materials show the properties of luminescence and the luminescent intensities are about 2 times of the bulk La_2O_3. They have the potentiality as luminescent materials.

Acknowledgment

The authors are grateful to the financial support from Changchun University of Science and Technology. The Grant number was XJJ2005-09.

References

[1] C.T. Kresge, M.E. Leonowicz, W.J. Roth, J.C. Vartuli, J.S. Beck, Nature 359 (1992) 710–712.
[2] A. Corma, Chem. Rev. 97 (1997) 2373–2420.
[3] J.H. Clark, Green Chem. 1 (1999) 1–4.
[4] B.M. Weckhuysen, R.R. Rao, J. Pelgrims, R.A. Schoonheydt, P. Bodart, G. Debras, O. Collart, P.V.D. Voort, E.F. Vansant, Chem. Eur. J. 6 (2000) 2960–2970.
[5] D.Y. Zhao, J.L. Feng, Q.S. Huo, N. Melosh, G.H. Fredrickson, B.F. Chmelka, G.D. Stucky, Science 279 (1998) 548–552.
[6] P.V.D. Voort, P.I. Ravikovitch, K.P.D. Jong, A.V. Neimark, A.H. Janssen, M. Benjelloun, E.V. Bavel, P. Cool, B.M. Weckhuysen, E.F. Vansant, Chem. Commun. 9 (2002) 1010–1011.
[7] U. Ciesla, F. Schuth, Micropor. Mesopor. Mater. 27 (1999) 131–149.
[8] C.A.S. Maria, X.S. Zhao, Appl. Surf. Sci. 237 (2004) 398–404.
[9] W. Chen, A.G. Joly, C.M. Kowalchuk, J.O. Malm, Y. Huang, J.O. Bovin, J. Phys. Chem. B 106 (2002) 7034–7041.
[10] H.R. Li, J. Lin, L.S. Fu, J.F. Guo, Micropor. Mesopor. Mater. 55 (2002) 103–107.
[11] J.R. Matos, L.P. Mercuri, J. Mietek, K. Michal, S. Yasuhiro, T. Osamu, J. Mater. Chem. 11 (2001) 2580–2586.
[12] M. Froba, R. Kohn, G. Bouffaud, O. Richard, V.G. Tendeloo, Chem. Mater. 11 (1999) 2858–2865.
[13] V.R. Choudhary, S.K. Jana, B.P. Kiran, J. Catal. 192 (2000) 257–258.
[14] Y.J. Han, J.M. Kim, G.D. Stucky, Chem. Mater. 12 (2000) 2068–2069.
[15] A. Fukuoka, Y. Sakamoto, S. Guan, S. Inagaki, N. Sugimoto, Y. Fukushima, K. Hirahara, S. Iijima, M. Ichikawa, J. Am. Chem. Soc. 123 (2001) 3373–3374.
[16] N.R.B. Coleman, M.A. Morris, T.R. Spalding, J.D. Holmes, J. Am. Chem. Soc. 123 (2001) 187–188.
[17] S. Zheng, L. Gao, Q.H. Zhang, J.K. Guo, J. Mater. Chem. 10 (2000) 723–728.
[18] M.S. Morey, G.D. Stucky, S. Schwarz, M. Froba, J. Phys. Chem. B 103 (1999) 2037–2041.
[19] K.K. Zhu, B. Yue, S.H. Xie, S.Y. Zhang, B. Zhang, S.L. Jin, H.Y. He, Chin. J. Chem. 22 (2004) 33–37.
[20] P. Chu, F. G. Dwyer, J. C. Vartuli, Crystallization method using microwave radiation, US Patent Application, No. 4 778 666, 1988
[21] U. Lohse, R. Bertram, K. Jancke, I. Kurzawski, B. Parlitz, E. Loeffler, E. Schreier, J. Chem. Soc. 91 (1995) 1163–1172.
[22] I. Girnus, K. Jancke, R. Vetter, M.J. Richter, J. Caro, Zeolites 15 (1995) 33–39.
[23] D.S. Kim, J.S. Chang, H. Wang, S.E. Park, J.M. Kim, Micropor. Mesopor. Mater. 68 (2004) 77–82.
[24] A. Arafat, J.C. Jansen, A.R. Ebaid, H.V. Bekkum, Zeolites 13 (1993) 162–165.
[25] C.G. Wu, T. Bein, Chem. Commun. 8 (1996) 925–926.
[26] M. Park, S. Komarneni, Micropor. Mesopor. Mater. 20 (1998) 39–44.
[27] L.N. Bharat, K. Sridhar, K. Hiroaki, Chem. Commun. (2000) 2389–2390.
[28] L.N. Bharat, O.L. Johnson, K. Sridhar, Chem. Mater. 13 (2001) 552–557.
[29] S. Brunauer, P.H. Emmett, E. Teller, J. Am. Chem. Soc. 60 (1938) 309–319.
[30] E.P. Barrett, L.G. Joyner, P.P. Halenda, J. Am. Chem. Soc. 73 (1951) 373–380.
[31] W.H. Hu, W. Wang, T.S. Jiang, C.L. Xia, Q.Z. Zhai, Chin. J. Spectr. Lab. 19 (2002) 434–436.
[32] Q.Z. Zhai, Y.C. Kim, Chin. J. Spectr. Lab. 15 (1998) 82–84.
[33] S.Y. Yu, L.P. Wang, B. Chen, Y.Y. Gu, J. Li, H.M. Ding, Y.K. Shan, Chem. Eur. J. 11 (2005) 3894–3898.
[34] IUPAC, Pure Appl. Chem. 87 (1957) 603–606.
[35] T.W. Kim, R. Ryong, K. Michal, P.G. Kamil, J. Mietek, K. Satoshi, T. Osamu, J. Phys. Chem. B 108 (2004) 11480–11489.
[36] M. Kruk, M. Jaroniec, J. Phys. Chem. B 106 (2002) 4732–4739.
[37] R.R. Xu, W.Q. Pang, Molecular Sieve and Porous Material Chemistry, Sci. Publish. House, Beijing, 2004, pp. 145–151.
[38] L. Vradman, M.V. Landau, D. Kantorovich, Y. Koltypin, A. Gedanken, Micropor. Mesopor. Mater. 79 (2005) 307–318.
[39] J.Y. Li, Luminescent Materials of Rare Earth and their Applications, Chemical Industry Publishing House, Beijing (2003) 154–160.
[40] T. Anastasiadou, L.A. Loukatzikou, C.N. Costa, A.M. Efstathiou, J. Phys. Chem. B 109 (2005) 13693–13703.
[41] H.Q. Liu, L.L. Wang, W.Q. Huang, Z.W. Peng, Mater. Lett. 61 (2007) 1968–1970.
[42] Z.G. Wei, L.D. Sun, C.S. Liao, C.H. Yan, Appl. Phys. Lett. 80 (2002) 1447–1449.
[43] J.J. Chang, S. Xiong, H.S. Peng, L.D. Sun, S.Z. Lu, F.T. You, S.H. Huang, J. Lumin. 122–123 (2007) 844–846.